Mineralogic and sulfur isotopic effects accompanying oxidation of pyrite in millimolar solutions of hydrogen peroxide at temperatures from 4 to 150 °C

Liliana Lefticariu *, Lisa M. Pratt, Edward M. Ripley

Department of Geological Sciences, Indiana University, Bloomington, IN 47405, USA

Received 5 December 2005; accepted in revised form 20 July 2006

Abstract

Oxidation of pyrite by hydrogen peroxide (H_2O_2) at millimolar levels has been studied from 4 to 150 °C in order to evaluate isotopic effects potentially associated with radiolytic oxidation of pyrite. Gaseous, aqueous, and solid phases were collected and measured following sealed-tube experiments that lasted from 1 to 14 days. The dominant gaseous product was molecular oxygen. No volatile sulfur species were recovered from any experiment. Sulfate was the only aqueous sulfur species detected in solution, with sulfite and thiosulfate below the detection limits. X-ray diffraction patterns and images from scanning electron microscopy reveal solid residues composed primarily of hydrated ferric iron sulfates and sporadic ferric–ferrous iron sulfates. Hematite was detected only in solid residue produced during high temperature experiments. Elemental sulfur and/or polysulfides are inferred to be form on reacting pyrite surface based on extraction with organic solvents. Pyrite oxidation by H_2O_2 increases in rate with increasing H_2O_2 concentration, pyrite surface area, and temperature. Rates measured in sealed-tube experiments at 25°C, for H_2O_2 concentration of 2×10^{-3} M are 8.8×10^{-9} M/m^2/sec, which are higher than previous estimates. A combination of reactive oxygen species from H_2O_2 decomposition products and reactive iron species from pyrite dissolution is inferred to aggressively oxidize the receding pyrite surface. Competing oxidants with temperature-dependent oxidation efficiencies results in multiple reaction mechanisms for different temperatures and surface conditions. Sulfur isotope values of remaining pyrite were unchanged during the experiments, but showed distinct enrichment of [34]S in produced sulfate and depletion in elemental sulfur. The $\Delta_{\text{sulfate–pyrite}}$ and $\Delta_{\text{elemental sulfur–pyrite}}$ was +0.5 to +1.5‰ and was −0.2 to −1‰, respectively. Isotope data from high-temperature experiments indicate an additional [34]S-depleted sulfur fraction, with up to 4‰ depletion of [34]S, in the hematite. Sulfur isotope trends were not influenced by H_2O_2 concentration, temperature, or reaction time. Results of this study indicate that radiolytically produced oxidants, such as hydrogen peroxide and hydroxyl radicals, could efficiently oxidize pyrite in an otherwise oxygen-limited environment. Although H_2O_2 is generally regarded as being of minor geochemical significance on Earth, the H_2O_2 molecule plays a pivotal role in Martian atmospheric and soil chemistry. Additional experimental and field studies are needed to characterize sulfur and oxygen isotope systematics during radiolytical oxidation of metallic sulfides and elemental sulfur.
© 2006 Elsevier Inc. All rights reserved.

1. Introduction

Radiation-induced chemical reactions have been extensively studied in the context of medical science and energy production but relatively little is known about the decay of long-lived, naturally occurring, radionuclides as a source of bioavailable chemical energy for microbes in the subsurface of Earth. Passage of ionizing radiation through water produces a complex mixture of short-lived ions, free radicals, and electronically excited molecules that can participate in a wide range of chemical reactions involving solutes and solids (e.g., Allen, 1961; Buxton, 1987; Garrett et al., 2004). In groundwater associated with uranium deposits, reactions between radiolytically produced radicals and aqueous or solid media result in complex mixtures of

* Corresponding author. Present address: Southern Illinois University, Carbondale, IL 62901. Fax: +1 812 855 7899.
   E-mail addresses: lleftica@indiana.edu, lefticariu@geo.siu.edu (L. Lefticariu).

oxidized and reduced products that can accelerate water-rock interaction (Vovk, 1987; Liu et al., 1996; Savary and Pagel, 1997; Burns and Hughes, 2003). Radiation-induced chemical reactions resulting in oxidation are particularly significant in geologic environments where molecular oxygen derived from the atmosphere is a negligible input. Results from geochemical studies of unconformity-related uranium deposits in Canada (Clarke and Fogwill, 1985; Bruneton, 1987; Fayek et al., 1997; Billault et al., 2002), roll-type uranium deposits (Vovk, 1982; Vovk, 1987) and Oklo nuclear fission zones (Dubessy et al., 1988; Savary and Pagel, 1997) indicate that radiolysis is considerably under-recognized as a naturally occurring source of chemical energy for biotic and abiotic reactions. In particular, radiolysis of water coupled to oxidation of sulfide minerals (Fayek et al., 1997) or elemental sulfur (Carlson et al., 2002) can produce gradients of partially to fully oxidized sulfur species that might be suitable for microbial metabolism.

Vovk (1987) suggested that wide ranges in sulfur isotope values of pyrite and groundwater sulfate in roll-front-type uranium deposits are related to a radiolytic process of oxidation, followed by disproportionation of intermediate sulfur species. No further experimental or field studies, however, have investigated fractionations of sulfur isotopes during radiolysis of water coupled to oxidation of sulfide minerals or elemental sulfur. Moreover, limited geochemical data are available from wells and springs for assessing the role of naturally occurring radionuclides on the oxidation of sulfide minerals and on subsequent formation of sulfate plumes in groundwater.

Hydrogen peroxide (H_2O_2) has been detected as a stable product of radiolysis in various natural environments. In anoxic subsurface environments associated with uranium deposits, H_2O_2 is inferred to be the principal stable oxidation species (Vovk, 1987; Liu et al., 1996). Peroxide-containing minerals such as studtite, $[(UO_2)(O_2)(H_2O)_2]$ $(H_2O)_2$, have been found in association with uranium deposits (Burns and Hughes, 2003; and references cited therein). Recent contributions suggest that H_2O_2 is a key catalytic component of the Martian atmosphere (Clancy et al., 2004) and an important oxidizing reactant in Martian regolith (Encrenaz et al., 2004). Elsewhere in the solar system, the chemical activity of H_2O_2 is inferred to be significant on the surface and beneath the ice cover of Jupiter's moon Europa (Chyba, 2000; Carlson et al., 2002; Gomis et al., 2004).

In this study, we evaluate radiolytic sulfide oxidation in the production of sulfate gradients and the stable isotope signatures of sulfur products in a series of sealed tube experiments using pyrite and H_2O_2 at temperatures from 4 to 150 °C. We used H_2O_2 as a proxy for radiolysis because H_2O_2 is the chief oxidizing molecular product formed during radiolysis of liquid water (Spinks and Woods, 1990; Garrett et al., 2004). At radiation doses representative of natural environments O_2 is probably insignificant (Pastina and LaVerne, 2001). In this study, we determined gaseous, aqueous, and solid products of abiotic pyrite oxidation in millimolar solutions of H_2O_2. Mineralogical, chemical, and stable isotopic data are used to infer multiple pathways for pyrite oxidation during reaction with H_2O_2. Oxidation is shown to be influenced by lattice defects in the starting pyrite and by the composition and distribution of intermediate sulfur products coating the pyrite surface. Significant variations in oxidation rate are attributed to experiment duration, temperature, and H_2O_2 concentration. These experiments are regarded as a starting point for modeling radiolysis as a source of bioavailable chemical energy in subsurface environments on Earth, Mars, and Europa.

2. Background

2.1. Experimental and environmental oxidation of pyrite

Pyrite is an abundant and widespread sulfide mineral on Earth forming in magmatic, metamorphic, or sedimentary settings. Extensive scientific study of pyrite has been driven by interest in (1) ecological impact of acid mine drainage (e.g., Alpers and Blowes, 1994; Evangelou, 1995; Nordstrom and Alpers, 1999), (2) microbial sulfate reduction as an indicator of oxygenation of Earth's atmosphere (e.g., Holland, 1994; Grotzinger and Knoll, 1999; Canfield et al., 2000; Ohmoto, 2004), (3) origin of life as a surface-mediated chemoautotrophic process (e.g., Wächtershäuser, 2000; Weiss et al., 2000), (4) economic impact of sulfur in ore bodies and hydrocarbons (e.g., Lowson, 1982) or for use as a photocatalyst (e.g., Chen et al., 1991), and (5) sulfide end products from microbial sulfate reduction (e.g., Sweeney and Kaplan, 1973; Brüchert and Pratt, 1996; Habicht et al., 1998; Canfield et al., 2000).

Pyrite oxidation is an electrochemical process involving cathodic electron transport and anodic reactions at the surface and apparently involving non site-specific multilayer adsorption of oxidant (Rosso et al., 1999a; Becker et al., 2001; Rimstidt and Vaughan, 2003; Borda et al., 2004). The cathodic reaction engages an aqueous species that accepts electrons from Fe atoms on the mineral surface. The anodic reaction involves removal of seven electrons from disulfide sulfur to form sulfate. Thus the sulfur atoms must pass through several oxidation states during the oxidation process with different sulfur compounds potentially involved (Luther, 1987; Moses et al., 1987; Williamson and Rimstidt, 1994; Kamei and Ohmoto, 1999; Rimstidt and Vaughan, 2003; Borda et al., 2004). In aerobic surface environments on Earth, the most important oxidants for pyrite are molecular oxygen, ferric ions, and water. Theoretical and experimental studies have shown that pyrite dissolution in aqueous environments is governed by the advection of the oxidant to pyrite surfaces (Rosso et al., 1999b; Kamei and Ohmoto, 1999; Rimstidt and Vaughan, 2003; Todd et al., 2003; Usher et al., 2005) with increased oxidation rates correlated to increased concentration of oxidant (McKibben and Barnes, 1986; Williamson and Rimstidt, 1994).

Stable-isotope fractionations associated with pyrite oxidation have been studied under abiotic and biotic conditions (Warren, 1972; Taylor et al., 1984; Toran and Harris, 1989; Krouse et al., 1991; Rye et al., 1992). Field studies of low-temperature oxidation of pyrite have found small sulfur isotope fractionations between starting sulfide mineral and resulting aqueous sulfate or sulfate minerals, generally not exceeding 3‰ (Taylor and Wheeler, 1994; Seal and Wandless, 1997; Budakoglu and Pratt, 2005). Biologically mediated experiments involving oxidation of aqueous sulfide in neutral to alkaline conditions have documented a negative sulfate–sulfide fractionation up to approximately 14‰ (Toran and Harris, 1989). It is not clear which mechanisms cause ^{34}S-enrichment of sulfates, but it has been suggested that a kinetic isotope effect could be linked to disproportionation of sulfur compounds of intermediate oxidation state rather than quantitative oxidation (Seal, 2003). Rapid, but abiotic, disproportionation of elemental sulfur to sulfate and sulfide has been proposed by Warren (1972) to explain ^{34}S-depleted pyrite in the ore-zone of roll-front sandstone-hosted uranium deposits.

Microbial disproportionation of intermediate sulfoxyanion species produced during sulfide oxidation (e.g., S^0, SO_3^{2-}, and $S_2O_3^{2-}$) causes preferential oxidation of ^{34}S and reduction of ^{32}S (Canfield, 2001). Culture studies of biological disproportionation of sulfur intermediates show fractionation values between 7 and 20‰, depending on the substrate (Canfield et al., 1998; Habicht et al., 1998; Bottcher et al., 2001). Relative contributions from abiotic and biotic processes to the overall fractionation of sulfur isotopes from different sulfur intermediates during pyrite oxidation are poorly constrained for Archean and Proterozoic setting on Earth.

2.2. Hydrogen peroxide as a proxy for radiolysis of water

Radiolytic decomposition of water produces a wide spectrum of radical and molecular products. Within a few picoseconds of an initial energy radiation event, water decomposition produces hydrated electrons e_{aq}^-, hydrogen (H) atoms, hydroxyl (HO$^\bullet$) radicals, and molecular hydrogen (H$_2$) in clusters along the particle path (Allen, 1961; Spinks and Woods, 1990). Within a few milliseconds, the principal oxidizing species are hydrogen peroxide (H$_2$O$_2$) and hydroxyl (HO$^\bullet$) radicals and the main reducing species are H atoms and H$_2$ molecules (Allen, 1961; Pastina and LaVerne, 2001). Upon continuous irradiation, steady-state concentrations of H$_2$O$_2$, H$_2$, and smaller amounts of dioxygen (O$_2$) are reached and no further decomposition occurs. H$_2$O$_2$ may be formed through the fast combination of hydroxyl (HO$^\bullet$) radicals (Buxton, 1987; Spinks and Woods, 1990).

The stability of H$_2$O$_2$ in solution is influenced primarily by temperature, pH conditions, and presence of impurities with a decomposing effect. H$_2$O$_2$ is stable in liquid water with losses of less than 1% per year at 25 °C. Rates of H$_2$O$_2$ decomposition increase with increases in temperature and with increases in pH value. Optimum H$_2$O$_2$ stability occurs at a pH below 4 and rapid decomposition occurs at a pH above 5. H$_2$O$_2$ is decomposed by radiation or light and decomposition can be promoted by numerous solid impurities even at low concentrations (Amme, 2002; Hiroki and LaVerne, 2005).

Hiroki and LaVerne (2005) proposed that the reaction mechanisms for thermal decomposition of H$_2$O$_2$ involves simple O–O bond cleavage to give two HO$^\bullet$ according to reaction 1, followed by two chain propagation reactions (reactions (2) and (3)).

$$H_2O_2 \rightarrow 2HO^\bullet \tag{1}$$

$$HO^\bullet + H_2O_2 \rightarrow HO_2^\bullet + H_2O \tag{2}$$

$$2HO_2^\bullet \rightarrow H_2O + O_2 \tag{3}$$

The overall reaction of H$_2$O$_2$ decomposition gives half of an O$_2$ molecule for every decomposed H$_2$O$_2$ molecule.

$$H_2O_2 \rightarrow H_2O + \tfrac{1}{2}O_2 \tag{4}$$

In some cases, such as in the presence of CeO$_2$ and ZrO$_2$, increases in H$_2$O$_2$ decomposition rates are dramatic (Petrik et al., 2001). Decomposition of aqueous solutions of H$_2$O$_2$ is accelerated by numerous solid impurities pointing to a variety of possible mechanisms (Petrik et al., 2001; Amme, 2002). Specific precursors to H$_2$O$_2$ decomposition are not known, and reaction mechanisms at surface or/and in bulk water remain enigmatic. Many mechanisms have been proposed with a notable commonality being decomposition in association with a solid interface (Hiroki and LaVerne, 2005).

Decomposition can be induced homogeneously by dissolved ions with transition metals like iron, copper, or nickel showing substantial catalytic effects. For example, the oxidation of redox-active ferrous ion (Fe^{2+}) by H$_2$O$_2$ is known as the Fenton reaction and results in formation of ferric ion (Fe^{3+}), hydroxyl (HO$^\bullet$) radicals, and hydroxyl (HO$^-$) ions.

$$Fe^{2+} + H_2O_2 \rightarrow Fe^{3+} + HO^\bullet + OH^- \tag{5}$$
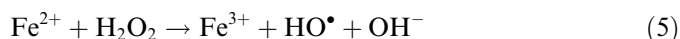
The Fenton reaction initiates a series of chain reactions, known as the Haber–Weiss cycle, in which H$_2$O$_2$ is consumed as followings:

$$H_2O_2 + HO^\bullet \rightarrow H_2O + O_2^{\bullet-} + H^+ \tag{6}$$

$$H_2O_2 + O_2^{\bullet-} + H^+ \rightarrow O_2 + HO^\bullet + H_2O \tag{7}$$
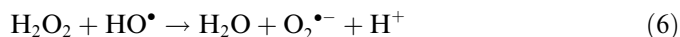
while chain termination is expressed by the reaction:

$$Fe^{2+} + HO^\bullet + H^+ \rightarrow Fe^{3+} + H_2O \tag{8}$$
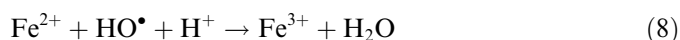
3. Experimental methods

3.1. Pyrite and solution preparation

Pyrite used in these experiments comes from quartz-pyrite veins in the Park City district of Utah. Pyrite was characterized by X-ray diffraction, ICP-MS analyses, and sulfur

Table 1
Chemical composition of Park City pyrite

Sample	Fe	S	Bi	Co	Ni	Cu	Zn	As	Se	Mo	Ag	Pb	U
EMR #1	45.72	52.82	5.77	240	7.4	39.6	7.1	113	182	1.64	2.55	140	0.2
EMR #2	43.95	50.17	31.4	170	8.8	1001	14.5	119	114	3.17	9.96	323	0.2
EMR #3	44.91	51.35	26.3	192	6.2	58.6	10.5	112	128	3.26	5.92	261	0.3

Fe and S in wt%; Bi, Co, Ni, Cu, Zn, As, Se, Mo, Ag, Pb, and U in ppm.

isotope analyses and was found to contain about 3% impurities, mainly quartz. The chemical composition of pyrite used in this study is presented in Table 1.

Previous studies indicate that mechanical breaking of pyrite crystals creates dangle bonds (Sasaki, 1994) resulting in increased oxidation of pyrite surfaces during crushing. For this reason, massive composite crystals of Park City pyrite were broken and individual intact pyrite crystals were hand picked. Prior to each set of experiments pyrite crystals were ground without water in an agate mortar and sieved; grain sizes in the range of 100–150 μm were segregated. This size fraction was submersed in an ultrasonic bath to disperse colloids, acid-washed with deoxygenated 0.1 M HNO_3, rinsed repeatedly with deoxygenated DI water, dried under N_2, and loaded in silica tubes.

Specific surface area of the cleaned pyrite was measured on a Quantosorb apparatus (Porous Media Co.) using the multipoint gas absorption technique (BET). Krypton was used for the absorption measurements at liquid nitrogen temperature. The specific average surface area of the 100–150 μm size fraction was 226 ± 6.5 cm^2/g. The experiments for this study were run using 60 mg of pyrite and 10 mL of solution, resulting in surface area to solution volume ratio (A/V) of 1.356 ± 0.03 cm^2/cm^3.

Standards and reagents were prepared using DI water prepared with a Milli-Q/Milli-Q Ultra Plus (>18 MΩ/cm) water system. DI water was purged with ultra pure Ar for at least 2 h. Following initial Ar purging, DI water was boiled under Ar atmosphere for 3–4 h and purged a second time with ultra pure Ar for an additional 2 h. A series of blank experiments were run using only Ar-purged deoxygenated DI water and pyrite at temperatures from 25 to 100 °C. Blank experiments were used to assess extraneous reactions. Over a period of 6 weeks, no sulfate minerals, elemental sulfur, or iron oxides were detected in solution or on pyrite surfaces from blank experiments.

3.2. Methodology

3.2.1. Experimental design

The experiments were conducted in silica tubes obtained from Quartz Plus Inc. Tubes were cut into 10 cm lengths and one end was sealed with a torch. Tubes were washed with dilute detergent, rinsed repeatedly with DI water, and baked for 24 h at 500 °C. Each tube was used only once.

About 60 mg of prepared pyrite was loaded in a clean silica tube. Immediately after loading, tubes were attached

to a vacuum line and evacuated to a pressure lower than 10^{-2} Pa using an Alcatel molecular-drag pump. An aliquot of 5 ml of deoxygenated DI water was injected into the tube through a septum port and the pyrite-water slurry was frozen by submersion of the tube in liquid nitrogen. Subsequently, an aliquot of 5 ml of H_2O_2 solution was injected into the tube while submerged in liquid nitrogen. The final concentration of H_2O_2 solution ranged from 0.002 to 0.2 M H_2O_2. The tubes were sealed with a torch under vacuum after all residual gases were evacuated. Sealed tubes were equilibrated quickly in water at a designated experimental temperature and transferred to an oven or refrigerator. Experiments were run at temperatures ranging from 4 to 150 °C with durations from 1 to 14 days. Duplicate and triplicate experiments were run to assess reproducibility of reaction products. Details of experimental combinations are presented in Table 2. At the end of experiments conducted above 25 °C, tubes were rapidly immersed in iced water to quench and stabilize products and remaining reactants.

3.2.2. Analysis of solutions

Several duplicate experiments were designed to measure the final pH and Eh values of the supernatant solution and the speciation in gaseous and aqueous phases. Sealed silica-tubes were opened on a vacuum line and gaseous species (noncondensable and condensable by liquid nitrogen) were collected. Determination of Eh and pH in the supernatant

Table 2
Record of pyrite oxidation experiments reported in this work, listing pertinent experimental conditions

Group	Experiment No.	[H_2O_2]$_0$ (M)	T range (°C)	Duration (days)
Group I	A # 8	0.2	4–150	1.5
	A # 9	0.2	4–150	2.5
	A # 10	0.2	4–150	3.5
	A # 11	0.2	4–150	7
	A # 12	0.2	4–150	10
	A # 13	0.2	4–150	14
Group II	A # 21	0.02	4–150	3.5
	A # 22	0.02	4–150	7
	A # 23	0.02	4–150	14
Group III	A # 31	0.002	4–150	3.5
	A # 32	0.002	4–150	7
	A # 33	0.002	4–150	14

The Group designation, related to the initial hydrogen peroxide concentration [H_2O_2]$_0$, is used throughout the text for reference to these conditions.

was done immediately after collection of gases. Electro-chemical parameters (pH and Eh) were collected and recorded after calibration (4 and 7 pH buffers and 1 Eh buffer) with a pH glass electrode (Radiometer XG250) and a Pt electrode (Radiometer XR110) each coupled with an Orion® Benchtop 250 A pH/mV meter. Aliquots of supernatant were filtered at 0.22 μm (Nalgene 190–2520) and immediately analyzed for sulfur and iron speciation. Aqueous sulfur speciation was determined by ionic chromatography on a Dionex analyzer ICS-2000 using an EGC II KOH as eluent generator and an IonPack AS11-HC column. $[Fe]_{total}$ was determined by furnace atomic absorption spectrometry (Perkin-Elmer Analyst 800, $\lambda = 248.3$ nm). Quantitative results of gaseous and aqueous species together with pH and Eh measurements are presented in Table 3.

3.2.3. X-ray diffraction, scanning electron microscopy, and electron microprobe analyses

For mineralogical and structural examination, tubes were equilibrated at room temperature and immediately opened. Supernatant liquid was extracted with a syringe and the solid residue was transferred to a quartz slide for X-ray diffraction or to a carbon tape for scanning electron microscopy. Both, XRD and SEM observations were made immediately after the tubes were open, on moist samples with no additional coating.

Mineral identification was determined using an X-ray diffractometer (Bruker, AXS D8 Advance). Samples were analyzed by Cu K-α radiation at an accelerating voltage of 45 kV and current of 35 mA. Data were collected in an angle range from 2° to 70°, and collection duration was tailored to each experiment with values between 1 and 48 h.

Table 3
Tabulated results of the pH and Eh values of the final supernatant solution, together with total iron concentration (molar) in supernatant solution and molecular oxygen gas (moles) collected at the end of 14 days experiments

Experiment No.	Experiment temperature (°C)	pH	Eh (mV)	Total Fe(aq) $\times 10^{-3}$ (M)	Total O_2 (moles)
A # 13	4	2.7	512	0.026	1.071
	25	2.7	450	0.036	1.025
	50	2.4	474	0.050	0.982
	100	2.2	464	0.002	0.839
	150	1.7	480	0.006	0.635
A # 23	4	3.2	448	0.013	0.200
	25	3.0	420	0.014	0.177
	50	2.7	482	0.022	0.167
	100	2.5	430	0.001	0.125
	150	2.1	450	0.005	0.040
A # 33	4	3.5	395	0.009	0.019
	25	3.3	392	0.012	0.017
	50	3.4	420	0.014	0.015
	100	2.6	415	0.020	0.011
	150	2.3	448	0.032	0.004

SEM observations were performed using a field emission scanning electron microscope FEI QUANTA 400 FEG instrument. Due to outgassing of hydroxide minerals during beam impaction, a low voltage of 2 kV was used as a balance between resolution and charge effect.

The composition of iron oxides was determined by wavelength dispersive analysis using a CAMECA SX50 electron microprobe at Indiana University. Major elements were determined using an accelerating voltage of 15 kV, a beam current of 20 nA and counting time of 20 s, and a beam size of 1 μm.

3.2.4. Sequential extraction of sulfur species

Sequential extraction of sulfur species yielded seven operationally defined fractions (Fig. 1), following a procedure modified from Brüchert and Pratt (1996). Supernatant solution and solid residue were separated by filtration using baked and dried 0.22 μm quartz-fiber filters (Whatman, QM-A). Dissolved sulfate was recovered from supernatant liquid by addition of 0.2 M $Ba(NO_3)_2$ solution and precipitation of $BaSO_4$. Recovered $BaSO_4$ was dried, weighed, and retained for isotope analysis (S_{aq} fraction). The filter and residue were returned to the silica tube and 20 ml of deoxygenated DI water was added. Tubes were capped and mixed on a shaking table for 2 h. After shaking, supernatant solution and solid residue were separated by filtration followed by repeated rinses with DI water. The second supernatant fraction included water-soluble sulfate minerals that were precipitated on the walls of the tube and on pyrite surfaces. Dissolved sulfate from minerals was recovered by addition of 0.2 M $Ba(NO_3)_2$ solution and precipitation of $BaSO_4$. Recovered $BaSO_4$ was dried, weighed, and retained for isotope analysis (S_{mn} fraction). The water-extracted residue was dried and solvent extracted for 48 h in a Soxhlet apparatus using dichloromethane (DCM). Copper granules were activated by rinsing with concentrated HCl and sequentially leaching with acetone, methanol, and dichloromethane. Activated copper was added to the Soxhlet flask to precipitate elemental sulfur and polysulfides as CuS. Coatings of CuS on copper were decomposed using dissolved hot 6 N HCl for four hours in a nitrogen-purged flask. Evolved H_2S was carried in flowing N_2 through a buffer solution (0.1 M citric acid adjusted to a pH of 3.5) into 0.1 M $AgNO_3$ trap. Precipitated Ag_2S was filtered, rinsed, dried, and saved for isotopic analysis (S_{el} fraction). The DCM-extracted residue was placed in a N_2 purged flask and 6N deoxygenated HCL was added slowly while stirring. Acid-volatile H_2S was transferred and collected (S_{av} fraction) as described above for copper coatings. The acidic solution containing acid-soluble sulfate was separated by filtration and sulfate was recovered (S_{as} fraction) as described above for water-soluble sulfate. The solid residue from acid extraction, representing the residual pyrite was dried, weighed, and retained for isotope analysis (S_{rp} fraction). Quantitative results for sequential extraction of sulfur species are presented in Table 4.
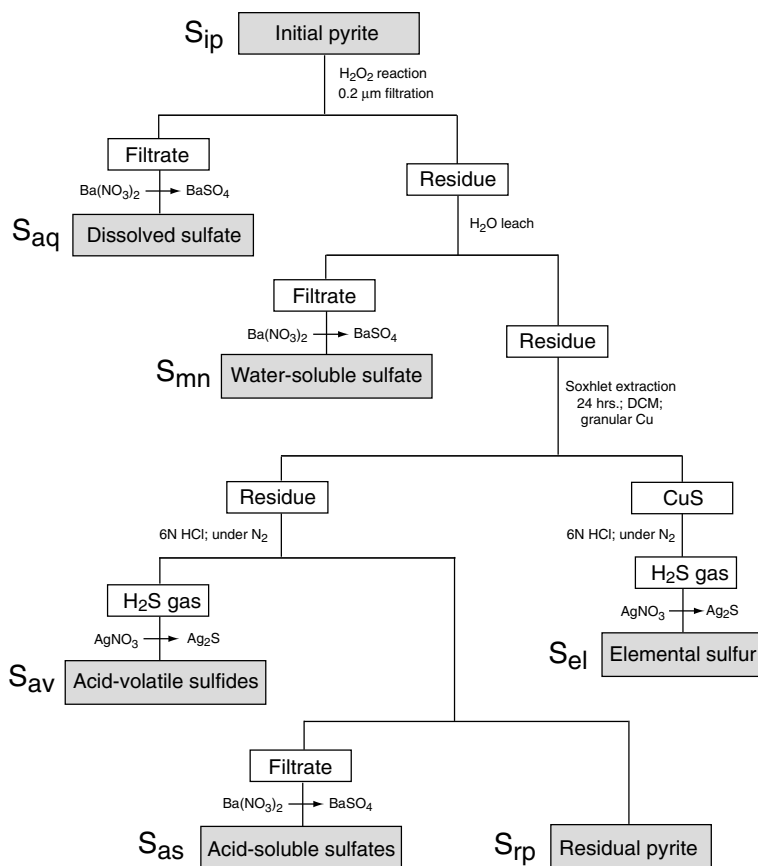
Fig. 1. Flowchart presenting the sequential extraction procedures used to quantify sulfur species resulted during pyrite oxidation by hydrogen peroxide that consists of seven operationally defined fractions: initial pyrite (S_{ip}), aqueous sulfate (S_{aq}), sulfate minerals (S_{mn}), elemental sulfur (S_{el}), acid-volatile sulfides (S_{av}), acid-soluble sulfate (S_{as}) and residual pyrite (S_{rd}). Procedure modified from Brüchert and Pratt (1996).

3.2.5. Stable isotopic measurements

A Finnigan MAT 252 mass spectrometer equipped with an elemental analyzer was used to determine sulfur isotopic compositions. Aliquots of initial and residual pyrite were analyzed directly as mineral powder. Produced sulfides and sulfates were analyzed as Ag_2S, and $BaSO_4$, respectively. Aliquots were loaded in tin cups, mixed with 1–2 mg of V_2O_5, and combusted on-line in a CE-1110 elemental analyzer at a flash temperature of 1400 °C. Combustion products were carried via He by continuous flow through a 1010 °C oxidation-reduction column, through a $MgClO_4$ water trap, and a Costech packed column (0.8 m) to purify SO_2. Isotopic compositions are reported in standard delta notation relative to V-CDT and are determined relative to the following standards: IAEA-S1 = −0.3‰, IAEA-S2 = +21.6‰, IAEA-S3 = −31.3‰, and NBS 127 = +20.3‰ (SO_2-scale). The overall analytical reproducibility is ±0.15‰. Sulfur isotopic data are presented in Table 4.

4. Results

Oxidation of pyrite by hydrogen peroxide can be described by the following generalized reaction:

$$FeS_2 + H_2O + H_2O_2 \rightarrow \text{residual } FeS_2 + \text{residual } H_2O$$
$$+ \text{solid products} + \text{aqueous products} + \text{gaseous products} \quad (9)$$
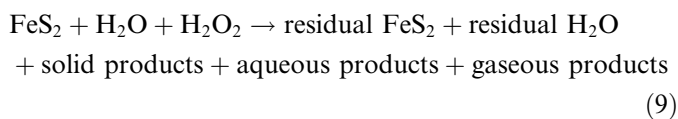
Sulfur species present as gaseous, dissolved, or solid phases were collected at the end of each experiment in order to quantitatively account for products of pyrite oxidation by H_2O_2. In addition to multiple sulfur species, we collected, identified, and measured several iron and oxygen species.

4.1. Species in gaseous and liquid phases

The chief gaseous species recovered from headspace in reaction tubes was molecular oxygen. Repeated measurements of headspace gasses did not yield detectable gaseous sulfur species. Sulfate was the only aqueous sulfur species detected by ion chromatography methods in supernatant solution. Species such as thiosulfate ($S_2O_3^{2-}$) and sulfite (SO_3^{2-}), expected to be stable in higher pH solutions (Goldhaber, 1983; Schippers and Jørgensen, 2001), were below detection limits. This observation is in agreement with other studies reporting that at pH < 4 intermediate sulfur species remain bond to pyrite surface until oxidation is complete and only sulfate is released into the solution

Table 4
Yields and isotopic composition of sulfur species for pyrite oxidation by H_2O_2

Group	Experiment No.	Temp (O °C)	S_{aq} fraction $S*10^{-3}$ (moles)	S_{mn} fraction $S*10^{-3}$ (moles)	S_{el} fraction $S*10^{-3}$ (moles)	S_{aq} fraction $\delta^{34}S_{aq}$ (‰)	S_{mn} fraction $\delta^{34}S_{mn}$(‰)	S_{el} fraction $\delta^{34}S_{el}$ (‰)	S_{rp} fraction $\delta^{34}S_{rp}$ (‰)
Group I $[H_2O_2]_0 = 0.2$ M	A # 8	4	0.213	—	<0.01	—	—	—	
		25	0.288	—	<0.01	—	—	—	
		50	0.340	—	<0.01	—	—	—	2.47
		100	0.494	—	<0.01	—	—	—	
		150	1.099	—	<0.01	—	—	—	
	A # 9	4	0.385	—	<0.01	3.29	—	—	
		25	0.426	—	<0.01	3.16	—	—	
		50	0.522	—	<0.01	2.98	—	—	2.47
		100	0.810	—	<0.01	2.83	—	—	
		150	1.731	—	<0.01	3.21	—	—	
	A # 10	4	0.481	<0.01	<0.01	2.99	—	2.26	2.44
		25	0.549	<0.01	<0.01	2.82	—	1.93	2.36
		50	0.683	<0.01	<0.01	2.87	—	2.12	2.49
		100	1.085	<0.01	<0.01	2.85	—	2.57	2.54
		150	2.294	<0.01	<0.01	2.95	—	1.65	2.33
	A # 11	4	0.907	0.002	0.893	2.97	3.07	2.23	2.31
		25	1.326	0.007	1.630	2.89	3.47	2.15	2.53
		50	1.690	0.010	0.932	2.89	3.15	1.65	2.47
		100	2.555	0.037	0.932	2.94	3.21	2.06	2.43
		150	4.904	0.121	1.358	3.02	3.41	2.23	2.56
	A # 12	4	1.219	0.004	0.880	3.03	3.18	1.53	2.33
		25	1.723	0.012	1.630	3.1	3.12	2.32	2.51
		50	2.290	0.020	0.880	2.92	3.14	2.03	2.62
		100	3.562	0.060	0.802	3.28	3.24	2.11	2.49
		150	7.112	0.230	0.725	3.36	3.02	1.94	2.53
	A # 13	4	1.635	0.058	0.670	2.95	3.28	1.58	2.49
		25	2.253	0.080	1.811	3.277	3.22	2.08	2.36
		50	3.091	0.101	1.449	2.94	3.04	2.34	2.54
		100	4.904	0.193	1.250	2.98	3.03	2.28	2.4
		150	10.055	0.371	1.183	2.94	3.21	1.44	2.55
Group II $[H_2O_2]_0 = 0.02$ M	A # 21	4	0.117	—	<0.01	—	—	—	
		25	0.129	—	<0.01	—	—	—	
		50	0.177	—	<0.01	—	—	—	2.47
		100	0.312	—	<0.01	—	—	—	
		150	0.535	—	<0.01	—	—	—	
	A # 22	4	0.440	—	0.906	2.71	—	1.52	2.32
		25	0.494	—	1.630	2.84	—	2.27	2.48
		50	0.563	<0.01	1.014	2.76	—	2.28	2.4
		100	1.236	<0.01	1.123	3.22	—	1.28	2.43
		150	1.648	<0.01	0.991	3.08	—	2.35	2.53
	A # 23	4	0.852	0.001	0.942	3.15	—	1.58	2.46
		25	0.920	0.003	1.723	3.34	—	1.74	2.66
		50	1.387	0.008	0.906	3.2	—	1.41	2.47
		100	2.198	0.023	1.051	3.15	—	1.48	2.52
		150	4.232	0.058	0.924	2.95	—	1.71	2.3
Group III $[H_2O_2]_0 = 0.002$ M	A # 31	4	<0.01	—	<0.01	—	—	—	
		25	<0.01	—	<0.01	—	—	—	
		50	<0.01	—	<0.01	—	—	—	2.47
		100	<0.01	—	<0.01	—	—	—	
		150	<0.01	—	<0.01	—	—	—	
	A # 32	4	0.169	—	0.652	—	—	2.22	2.24
		25	0.212	—	1.831	—	—	2.17	2.44
		50	0.252	—	0.916	—	—	2.28	2.56
		100	0.402	—	1.087	—	—	2.40	2.38
		150	0.710	—	1.257	—	—	2.17	2.51
	A # 33	4	0.591	—	0.543	3.09	—	1.93	2.50
		25	0.769	—	1.449	3.21	—	2.03	2.38
		50	0.926	—	1.087	2.99	—	2.16	2.59

Table 4 (continued)

Group	Experiment No.	Temp (O °C)	S_{aq} fraction $S*10^{-3}$ (moles)	S_{mn} fraction $S*10^{-3}$ (moles)	S_{el} fraction $S*10^{-3}$ (moles)	S_{aq} fraction $\delta^{34}S_{aq}$ (‰)	S_{mn} fraction $\delta^{34}S_{mn}$(‰)	S_{el} fraction $\delta^{34}S_{el}$ (‰)	S_{rp} fraction $\delta^{34}S_{rp}$ (‰)
		100	1.717	—	1.195	2.91	—	1.35	2.36
		150	2.472	—	1.190	2.89	—	1.34	2.49

Sequential extraction procedures resulted in the recovery of aqueous sulfate (S_{aq} fraction), sulfate mineral (S_{mn} fraction) and sulfur/polysulfide (S_{el} fraction). Acid-volatile sulfide (S_{av} fraction) and acid-soluble sulfate (S_{as} fraction) were not recovered from any experiment. No volatile sulfur species were recovered from any experiment. The final mass of each sulfur species was converted into equivalent weight (in moles) of elemental sulfur. Sulfur isotope values are presented for aqueous sulfate (S_{aq} fraction), sulfate minerals (S_{mn} fraction), elemental sulfur (S_{el} fraction), and residual pyrite (S_{rd} fraction).
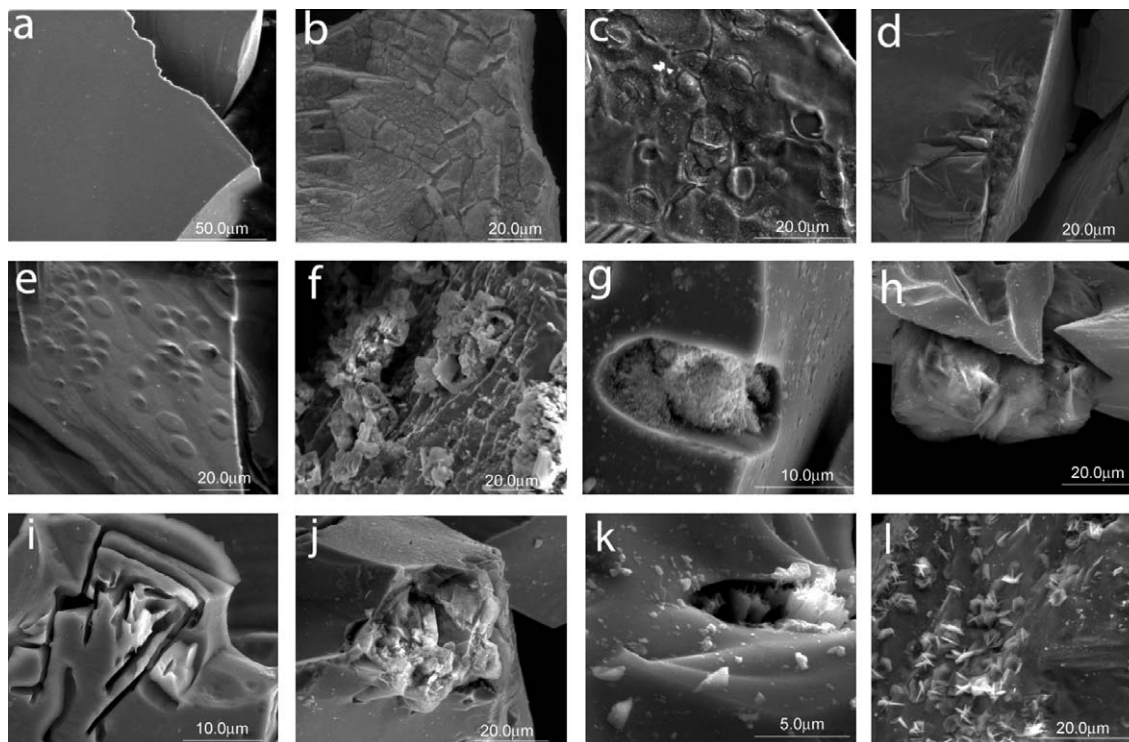
Fig. 2. SEM photomicrographs of acid-cleaned initial pyrite (a) and residual pyrite at the end of Group I experiments run (b) and (c) at 4 °C; (d) and (e) at 25 °C; (f) and (g) at 50 °C; (h) and (e) at 100 °C; and (j), (k), and (l) at 150 °C. X-ray measurements detected only iron sulfate minerals on the residual pyrite. At low reaction temperatures (e.g., 4–50 °C), the hydrated iron sulfates remain mainly on pyrite surface forming an alteration crust. At high temperatures (e.g., 100–150 °C), the iron sulfates crystallize on pyrite surfaces or in pits formed during pyrite dissolution.

(e.g., Moses et al., 1987; Bonnissel-Gissinger et al., 1998; Rimstidt and Vaughan, 2003; Todd et al., 2003). Yields of aqueous sulfate expressed as sulfur equivalent are up to 33% of sulfur in initial pyrite (Table 4). In all experiments, the final mass of each sulfur species was converted into equivalent weight (in moles) of elemental sulfur with results tabulated in Table 4.

4.2. Mineralogy and surface features of the solids

Acid-cleaned pyrite was characterized by XRD and SEM methods. XRD scans of the initial solid revealed only pyrite. SEM observations showed flat surfaces, sharp edges, and concoidal fractures on the initial pyrite crystals (Fig. 2a), with some grains having small linear fractures inferred to result from crushing.

Changes in solid mineralogy and morphology were monitored for each group of experiments using duplicate runs. SEM images revealed a wide range of surface and edge features of the final solid residue, with distinct texture and crystal morphologies mapped for experiments run under different initial conditions (Figs. 2b–l). Among all of the variables, temperature appears to have the strongest influence on morphology of residual pyrite and sulfate mineral phases. In experiments run at 4 and 25 °C, residual pyrite surfaces were completely covered by submicrometer-sized grains of Fe-sulfate minerals in a multi-layered crust (Figs. 2b–e). In experiments run at higher temperature, micrometer-sized crystals and aggregates of crystals adhered to residual pyrite surfaces and edges. Crystal aggregates are irregular to spherical and individual euhedral crystals are bladed to fibrous or acicular. Minerals

produced during hydrogen peroxide oxidation usually occur in polyphase aggregates which is consistent with observations from Todd et al. (2003) and Jerz and Rimstidt (2004) of iron sulfate mixtures on surfaces of oxidized pyrite samples (Fig. 2f–l). Interestingly, sulfate minerals were present regardless of the concentration of sulfate in solution. Sulfate concentration gradients are expected within the tubes. Sulfate saturation near the pyrite surface and sulfate concentration decreasing into the solution would favor formation of sulfate minerals near/on pyrite surfaces.

XRD analyses of the solid residue analyzed immediately after opening the reaction tubes show peaks characteristic of numerous crystalline phases in addition to pyrite. Most of the minerals identified by XRD correspond to iron sulfates. Ferric sulfate minerals include rhomboclase $[(H_5O_2)^+Fe^{3+}(SO_4)_2 \cdot 2(H_2O)]$, kornelite $[Fe_2^{3+}(SO_4)_3 \cdot 7(H_2O)]$, hydroniumjarosite $[(H_3O^+)_2Fe_6^{3+}(SO_4)_4(OH)_{12}]$, rozenite $[Fe^{3+}SO_4 \cdot 4(H_2O)]$, and coquimbite $[Fe_2^{3+}(SO_4)_3 \cdot 9(H_2O)]$. In addition, a ferric–ferrous hydrated iron sulfate, copiapite $[Fe^{2+}Fe_4^{3+}(SO_4)_6(OH)_2 \cdot 20(H_2O)]$, was identified. The submicrometer size of many sulfate crystals inhibited identification of specific mineral phases using the SEM and, consequently, no definitive correlation between temperature and product mineralogy could be established.

Elemental sulfur (S^0), polysulfides (FeS_n), and metal-deficient sulfide ($Fe_{1-x}S_2$) were produced on pyrite surface and collected by sequential extraction (Table 4). These types of sulfur species are often referred to as S^0-like or sulfur-rich species and suggested as intermediate products of pyrite oxidation (Buckley and Riley, 1991; Sasaki et al., 1995; Bonnissel-Gissinger et al., 1998; Nesbitt et al., 1998; Kamei and Ohmoto, 1999). Elemental sulfur was not detected by XRD methods for any experiment despite recovery of elemental sulfur from many experiments by sequential extraction. The formation of a sulfur-rich surface during pyrite oxidation is predicted by theoretical models (Luther, 1987; Rimstidt and Vaughan, 2003) and documented by surface studies (Mycroft et al., 1990; Nesbitt et al., 2000; Todd et al., 2003; Kendelewicz et al., 2004). Enrichment in surface sulfur is inferred to represent the first step in a series of elementary surface reactions in which sulfur-bond disulfide is stepwise oxidized to sulfate.

In experiments run at 100 and 150 °C, hematite [Fe_2O_3] was identified by XRD from bright-red precipitates that formed as coating on the silica-tube walls. Hematite was the only iron oxide mineral identified in solid residues. Even though the Fe^{3+}-bearing oxidation products are highly soluble, initial nucleation and growth of hematite crystals below pH of 3.5 in high-temperature experiments could have been promoted by the presence of favorable nucleation sites on the silica tube surface. Additional electron microprobe measurements of hematite coatings revealed sulfur concentrations ranging from 7 to 12 wt% sulfur. It is not clear if sulfur is present as sub-micron inclusions in hematite lattice defects or as substitution for O^{2-} in hematite lattice.

4.3. Oxidation trends

Dependence of oxidation reaction on initial H_2O_2 concentration, $[H_2O_2]_0$, was investigated over a temperature range from 4 to 150 °C and a time interval of 1.5–14 days. H_2O_2 concentrations were 0.2 M for Group I experiments, 0.02 M for Group II experiments, and 0.002 M for Group III experiments (Table 2).

For each $[H_2O_2]_0$ there is a linear increase of aqueous sulfate yield (S_{aq} fraction) with time for each temperature of reaction considered, and a higher yield at higher temperature (Fig. 3). Nearly identical rates of aqueous sulfate production (S_{aq} fraction) were measured for Group I ($[H_2O_2]_0 = 0.2$ M) experiments over 1.5–14 days (Fig. 4a) suggesting that similar mechanisms operated for aqueous sulfate production at each specific temperature (Fig. 4a). We did not measure any changes in aqueous sulfate production with time of reaction as reported in other studies (Jerz and Rimstidt, 2004). Even in low-temperature, long-duration experiments in which pyrite surfaces were completely covered by sulfate minerals (Fig. 2 b, c, and f), the measured rates were consistent.

For all three groups of experiments, an exponential increase in aqueous sulfate production was measured with increasing temperature and individual average rates were strongly dependent on $[H_2O_2]_0$ (Fig. 4b). The aqueous sulfate yield is also directly dependent on $[H_2O_2]_0$ (Fig. 4b). Similar positive correlations between produced sulfate minerals (S_{mn} fraction), temperature, and time were revealed by sequential extraction measurements and SEM observations (Table 4). These trends were observed in all experiments, regardless of the $[H_2O_2]_0$ or the concentration of produced sulfate in solution.

Dissimilar trends were obtained for sulfur/polysulfide yield (S_{el} fraction) compared to aqueous sulfate yield (S_{aq} fraction) and sulfate mineral yield (S_{mn} fraction). The sulfur/polysulfide yields do not appear to correlate with $[H_2O_2]_0$ or temperature of reaction (Fig. 5a). The lowest yields were recovered from experiments run at 4 °C. Similar
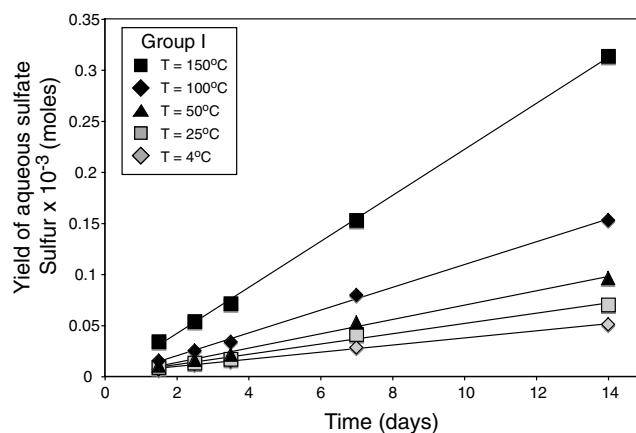
Fig. 3. Comparison of yields of aqueous sulfate (S_{aq} fraction) for Group I experiments run at temperature from 4 to 150 °C. There is a linear increase in yield of aqueous sulfate with time, for each temperature considered.
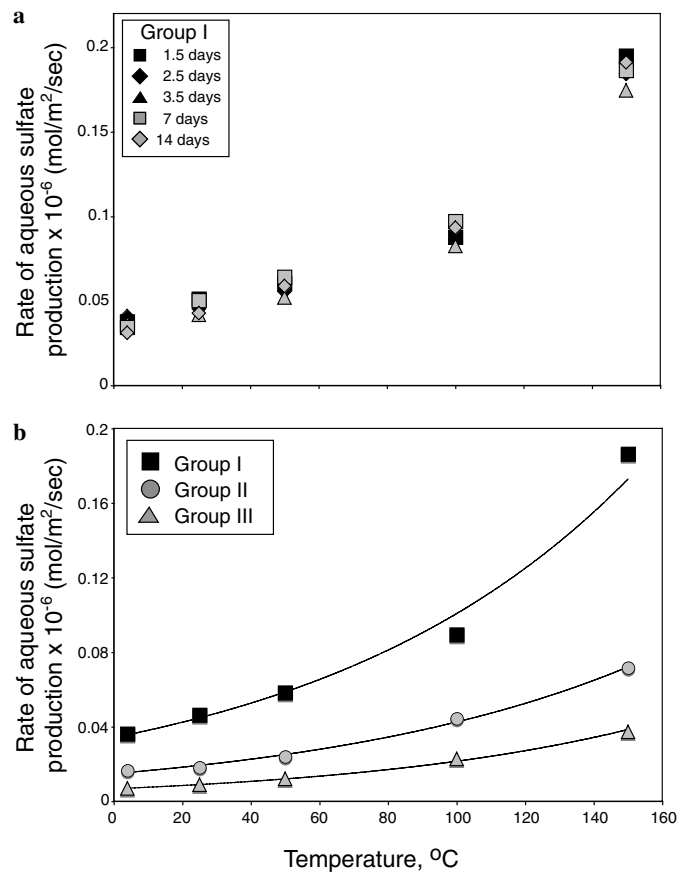
Fig. 4. Comparison of rates of aqueous sulfate (S_{aq} fraction) production as a function of temperature of reaction. (a) Rates of aqueous sulfate production for Group I experiments run at temperature from 4 to 150 °C and time intervals of 1.5–14 days. Similar rates were measured for each temperature considered, regardless of the experiment duration. (b) Average rates of aqueous sulfate production for Group I, II, and III experiments (data from Table 4). Rates of aqueous sulfate production covary with $[H_2O_2]_0$ and temperature. There is an exponential increase in rates of aqueous sulfate production, for each temperature considered, regardless of the $[H_2O_2]_0$.

ranges of yield values were found from experiments run at temperature of 25 °C and higher (Fig. 5a). The yield rate of elemental sulfur is, however, dependent on time. Rates up to two times higher were measured in 7-day experiments compared to 14-day experiments (Table 4 and Fig. 5b).

Acid-volatile sulfide (S_{av} fraction) and acid-soluble sulfate (S_{as} fraction) were not recovered from any experiment. Overall, aqueous sulfate (S_{aq} fraction) and elemental sulfur (S_{el} fraction) represent the most significant fractions of pyrite oxidation products.

To examine variation of pyrite dissolution rate as a function of temperature and $[H_2O_2]_0$, we consider the total sulfur release as represented by the sum of aqueous sulfate yield (S_{aq} fraction) and sulfate mineral yield (S_{mn} fraction). An average rate of pyrite dissolution for each group of experiments was calculated based on the total sulfur release with results presented in Table 5 and plotted in Figs. 6 and 7. Fig. 6 shows that rates of pyrite dissolution correlate exponentially with temperature of reaction. Measured
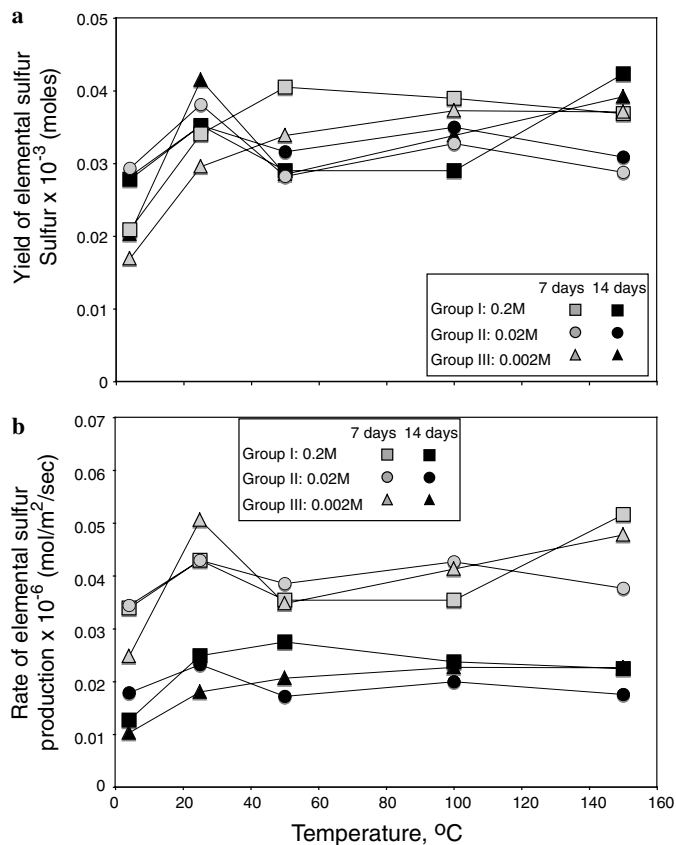
Fig. 5. Comparison of (a) yields of elemental sulfur and (b) rate of elemental sulfur production for Group I, II, and III experiments run at temperature from 4 to 150 °C and time intervals of 7 and 14 days. The yield of elemental sulfur/polysulfide does not correlate with $[H_2O_2]_0$ or temperature. Data tabulated in Table 4.

dissolution rates ranged from 4.5×10^{-8} mol/m²/s to 6.9×10^{-9} mol/m²/s at 4 °C, and from 2.2×10^{-7} mol/m²/s to 3.2×10^{-8} mol/m²/s at 150 °C (Table 5). Results from experiments run at temperature higher than 50 °C show that increased temperature causes a marked increased in dissolution rate. In addition, rates of pyrite dissolution are directly dependent on the $[H_2O_2]_0$ regardless of reaction temperature (Fig. 7).

4.4. Sulfur isotopic values

Repeated analyses during 2001–2005 of the Park City pyrite used for these experiments shows isotopic homogeneity with respect to $\delta^{34}S$ values. An average $\delta^{34}S$ value of $2.42 \pm 0.15‰$ was obtained over the 1-year duration of pyrite oxidation experiments. Results of sulfur isotopic measurements of initial pyrite and recovered sulfur fractions are summarized in Table 4 and plotted in Fig. 8. Values of $\delta^{34}S$ range from $+2.8‰$ to $+3.3‰$ for the aqueous sulfate fraction (S_{aq}), from $+3.0‰$ to $+3.5‰$ for the soluble sulfate mineral fraction (S_{mn}), and from $+1.4‰$ to $+2.3‰$ for the elemental sulfur/polysulfide fraction (S_{el}). A direct comparison among different sulfate mineral phases visible with SEM on pyrite surfaces was not possible due to

Table 5
Calculated rates of pyrite dissolution

Experiment temperature (°C)	Rate of pyrite dissolution (mol/m²/s)		
	Group I $[H_2O_2]_0 = 0.2$ M	Group II $[H_2O_2]_0 = 0.02$ M	Group III $[H_2O_2]_0 = 0.002$ M
4	4.50×10^{-8}	1.65×10^{-8}	6.89×10^{-9}
25	6.02×10^{-8}	2.13×10^{-8}	8.85×10^{-9}
50	7.87×10^{-8}	2.82×10^{-8}	1.19×10^{-8}
100	1.21×10^{-7}	4.46×10^{-8}	2.00×10^{-8}
150	2.24×10^{-7}	7.21×10^{-8}	3.20×10^{-8}
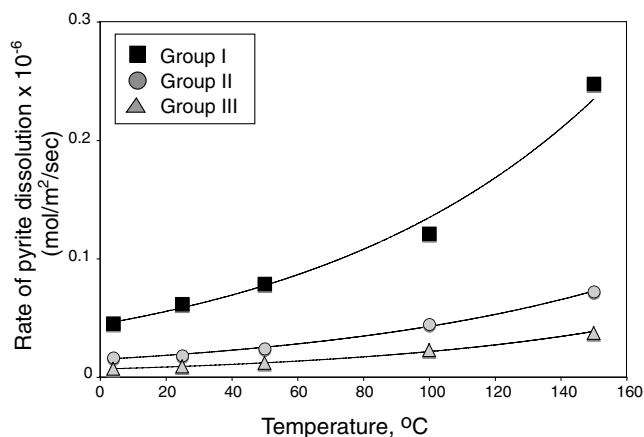
Fig. 6. Comparison of average rates of pyrite dissolution for Group I, II, and III experiments run at temperature from 4 to 150 °C. Rates were determined on the basis of total sulfate production as represented by the sum of aqueous sulfate yield (S_{aq} fraction) and sulfate mineral yield (S_{mn} fraction). Average rate values increase exponential with temperature of reaction.
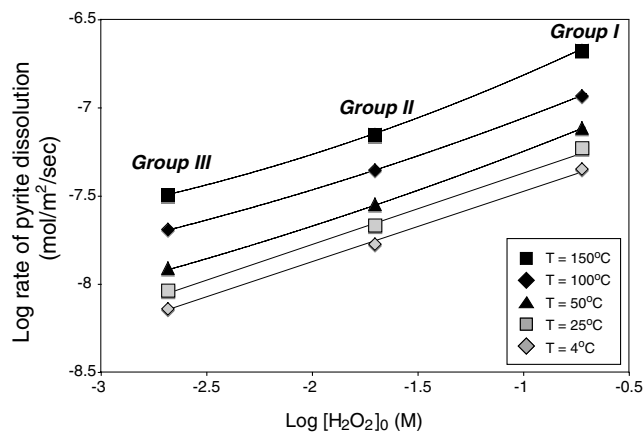
Fig. 7. Values of the log rate of pyrite dissolution *vs.* log $[H_2O_2]_0$ for Group I, II, and III experiments run at temperature from 4 to 150 °C. At low temperature (4 and 25 °C), pyrite dissolution varies by approximately 10^{-8}–10^{-9} mol/m²/s in a linear fashion. The linear fit of log rate *vs.* log $[H_2O_2]_0$ indicates that rates of pyrite dissolution are first order with respect to $[H_2O_2]_0$. Deviation from linear dependence is observed at reaction temperature of 50 °C and higher, and assumption of a first order rate is not valid.

the micron to submicron size of crystal aggregates (e.g., Fig. 2g, h, and j). $\delta^{34}S$ values of disseminated sulfur in hematite flakes vary from −1.6‰ to +1.4‰.
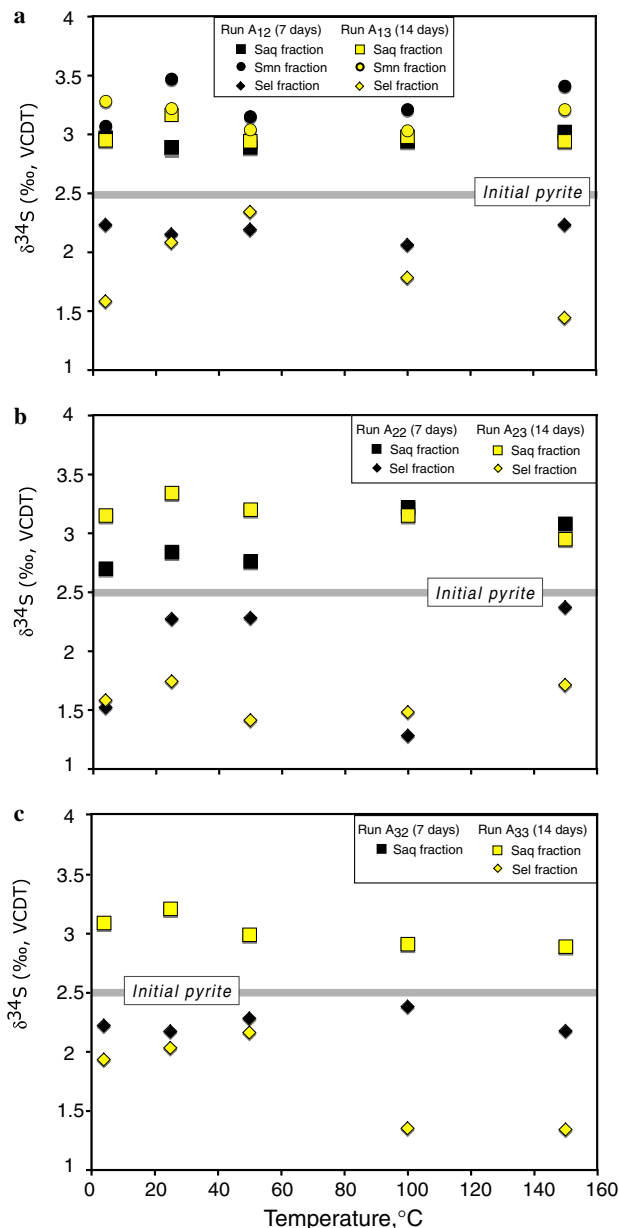
Fig. 8. Sulfur isotope data for: (a) Group I, (b) Group II, and (c) Group III experiments run at temperature from 4 to 150 °C. $\delta^{34}S$ remained unchanged for pyrite but showed distinct enrichment of ^{34}S in produced sulfate (Δsulfate–pyrite is 0.5–1.5‰) and depletion in elemental sulfur (Δpyrite–elemental sulfur is up to 1‰). No correlation could be established between sulfur isotope data and $[H_2O_2]_0$, temperature, or experiment duration. Data tabulated in Table 4.

Residual pyrite (S_{rp}) has an average $\delta^{34}S$ value of 2.47 ± 0.15‰ and is isotopically indistinguishable from initial pyrite. The aqueous sulfate fraction is heavier by 0.5–1‰ than initial pyrite and the soluble sulfate mineral fraction is heavier by 0.8–1.5‰ than initial pyrite (Table 4, Fig. 8). The elemental sulfur/polysulfide fraction is depleted in ^{34}S by up to 1‰ than initial pyrite (Table 4, Fig. 8). Unexpectedly, values of $\delta^{34}S$ for recovered aqueous and mineral sulfur fractions, and residual pyrite did not display any detectable dependence on experimen-

tal temperature, $[H_2O_2]_0$, pyrite grain size or reaction duration.

5. Discussion

The key finding of this work is that pyrite is readily oxidized by millimolar solutions of H_2O_2 in an otherwise oxygen-free environment. H_2O_2 was used in this study as a proxy for radiolytically produced oxidants, because H_2O_2 is the main oxidizing species produced during water radiolysis and not molecular oxygen (Allen, 1961; Pastina and LaVerne, 2001). Experimental results show that the dominant sulfur products during oxidation of pyrite by H_2O_2 are aqueous sulfate, hydrated iron sulfates, and elemental sulfur. Rates of pyrite oxidation by H_2O_2 increase with increasing $[H_2O_2]_0$ and increasing temperature of reaction.

5.1. Oxidation of pyrite by H_2O_2

During initial interaction between H_2O_2 and pyrite surfaces, H_2O_2 dissociates generating molecular oxygen (O_2) and highly reactive species such as hydroxyl radical ($HO^\bullet$), perhydroxyl radical ($HO_2^\bullet$), superoxide radical anion ($O_2^{\bullet-}$), and hydroperoxide (HO_2^-) (Hiroki and LaVerne, 2005). Although dissociation rates for H_2O_2 are a function of temperature, the presence of a solid surface accelerates the process at any temperature (Amme, 2002; Stefanic and LaVerne, 2002). Our measurements indicate that H_2O_2 decomposes readily on pyrite surfaces and at least half of the initial H_2O_2 dissociates to form O_2 (Table 3). Pyrite that reacted with deoxygenated DI water under the same experimental conditions as H_2O_2 experiments showed no detectable surface alteration, and no dissolved sulfur species identified in the supernatant solution, suggesting minimal reactions in the absence of H_2O_2. Given that water simply physisorbes molecularly to the pyrite surface (Guevremont et al., 1998; Rosso et al., 1999b), the presence of an active oxidizing species is critical in initiating pyrite oxidation in an anoxic environment.

The most important oxidizing species resulting from H_2O_2 dissociation is inferred to be the hydroxyl radical ($HO^\bullet$) which is one of the most reactive chemical species known, second only to elemental fluorine in its reactivity. Oxidation of pyrite appears to occur by direct reaction between $HO^\bullet$ and the disulfide groups on the pyrite surface. Previous studies have shown that $HO^\bullet$ could affect oxidation kinetics of intermediate sulfur species formed during stepwise oxidation of pyrite, such as sulfite (Ermakov et al., 1997), trithionate and tetrathionate (Druschel et al., 2004), and thiosulfate (Schöneshöfer, 1973). In solution, $HO^\bullet$ can initiate a series of free radical chain reactions involving Fe^{2+} and H_2O_2, conforming to reactions (5)–(8), with the production of Fe^{3+}, O_2, and H_2O. Secondary pyrite oxidation reactions involving Fe^{3+} and O_2 are consistent with previously published studies of pyrite reactivity (McKibben and Barnes, 1986; Moses et al., 1987; Williamson and Rimstidt, 1994; Kamei and Ohmoto, 1999).

Overall, dissolution of pyrite in aqueous solution is not a homogeneous process. Initially, oxidation is highly favored by the presence of structural defects, inclusions, and cleavage-induced surface damages (Guevremont et al., 1998; Schaufuss et al., 1998). Selective dissolution sites further increase the reactive surface area leading to rapid development of discrete oxidation patches (Fig. 2g, h, and j). Accordingly, the number and efficiency of active sites rather than the total surface area are critical during initial oxidation processes. The growth of sulfate minerals promotes fracturing and weakening of the pyrite crystal (Fig. 2h and j), due to a significant volume increase per unit of sulfur (Jerz and Rimstidt, 2004).

Stoichiometric constrains on overall reactions for pyrite oxidation by H_2O_2 were achieved using quantitative measurements of soluble and solid sulfur species (Table 4) combined with data on speciation and yields of gaseous species (e.g., O_2) as well as pH and Eh of final solutions (Table 3). Mass balance calculations indicate that during oxidation of pyrite by H_2O_2 most of disulfide sulfur in pyrite is converted to sulfate. Decomposition of H_2O_2 produces oxidized species such as $HO^\bullet$ and O_2, and reduced species such as H^+, which contributes to a sharp decrease in solution pH (Table 3).

5.2. Oxygen budget

Molecular oxygen was the chief gas collected at the end of each experiment. Amounts of O_2 collected were dependent on $[H_2O_2]_0$ and temperature of reaction. Regardless of $[H_2O_2]_0$, measured amounts of O_2 at the end of 14-day experiments decreased with increasing reaction temperature (Fig. 9). This trend is further correlated with increasing yield of sulfate production at high temperature (Fig. 10).

An unexpected result of our study is the finding that oxygen budgets cannot be balanced if H_2O_2 is the only spe-
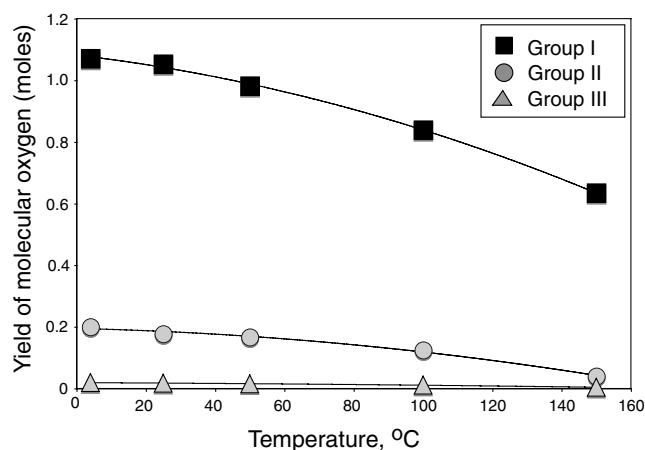
Fig. 9. Comparison of yield of molecular oxygen recovered at the end of 14 days for Group I, II, and III experiments (Table 3). The measured amount of O_2 at the end of 14-day experiments decreases with increasing reaction temperature, regardless of $[H_2O_2]_0$.
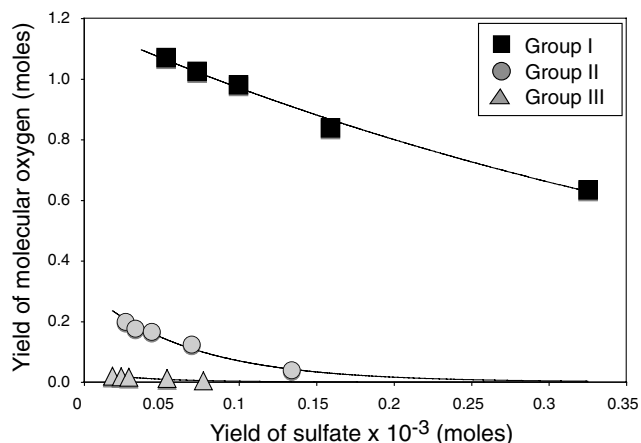
Fig. 10. Yield of molecular oxygen relative to yield of sulfate collected at the end of 14-days for Group I, II, and III experiments. Data from Table 3.

cies contributing oxygen to pyrite oxidation products. Fig. 11 shows an oxygen mass balance in which the only input oxygen species is H_2O_2. For Group I experiments, mass balance calculations indicate that oxygen in initial H_2O_2 can account for all oxygen in gaseous, aqueous, and solid products. For Group II and III experiments, however, oxygen in initial H_2O_2 cannot balance total oxygen in oxidation products. Thus, water is probably contributing oxygen to pyrite oxidation products.

Experimental results and modeling calculations suggest a combined role of molecular oxygen and water for effective oxidation of pyrite (Rosso et al., 1999b, Borda et al., 2004; Jerz and Rimstidt, 2004; Usher et al., 2005). As our results show, water plays a key role in oxidation of pyrite by H_2O_2. This finding is in agreement with results of other studies of pyrite oxidation (Reedy et al., 1991; Taylor and Wheeler, 1994; Usher et al., 2005), which indicated that
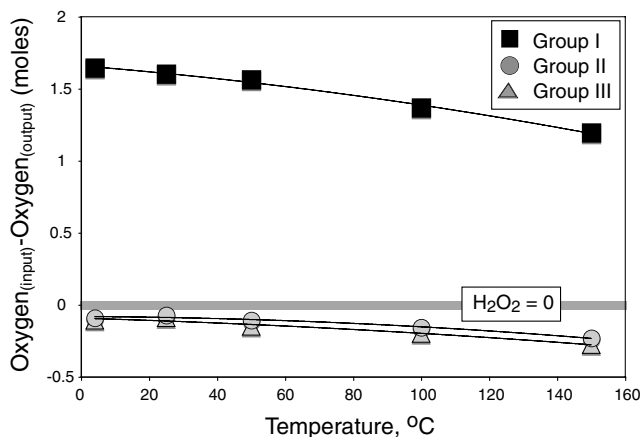
Fig. 11. Graph of oxygen mass-balance calculations for Group I, II, and III experiments in which the only input oxygen species is H_2O_2. For Group I experiments the mass balance calculations indicate that the oxygen in the initial H_2O_2 can account for the oxygen in the gas, aqueous, and solid pyrite oxidation products. For Group II and III the oxygen in the initial H_2O_2 cannot balance the total oxygen in the pyrite oxidation products.

oxygen in produced sulfate is dominantly derived from water.

Based on our current database we are unable to differentiate the source(s) of oxygen and to determine the ratios of oxygen derived from H_2O_2 and water in various pyrite oxidation products. Future [18O]-labeled experiments are needed to clarify the mechanisms of pyrite oxidation by H_2O_2.

5.3. Reaction rates of pyrite oxidation by H_2O_2

Rates of pyrite dissolution were determined on the basis of total sulfate production for each group of experiments at different temperature of reaction (Table 5). Measured average pyrite dissolution rates at 25 °C are in the range of 10^{-8} to 10^{-9} M/m^2/sec assuming a physical surface area equal to the BET values of 226 cm^2/g (Table 5). After data are corrected for specific solid/liquid ratio, the rate found by this study of 8.8×10^{-9} M/m^2/sec at a $[H_2O_2]_0$ of 2×10^{-3} M at 25 °C is slightly higher than the rate reported by McKibben and Barnes (1986) of 5.4×10^{-9} M/m^2/sec. This discrepancy is not significant and can be explained by different experimental conditions for the two studies. The batch reactor used by McKibben and Barnes (1986) was purged with nitrogen gas during the duration of experiments, allowing molecular oxygen produced during H_2O_2 dissociation to escape. Our experimental designed used sealed silica tubes and prevented the escape of oxygen produced during H_2O_2 decomposition, allowing oxidants (e.g., O_2) to be conserved within the system.

The dependence of pyrite dissolution rate on $[H_2O_2]_0$ is subtly complex. At low temperature (4 and 25 °C), pyrite dissolution varies by approximately 10^{-8}–10^{-9} mol/m^2/s in a linear fashion (Fig. 7). The linear fit of log rate *vs.* log $[H_2O_2]_0$ indicates that rates of sulfate production are first order with respect to $[H_2O_2]_0$, in agreement with previous results reported by McKibben and Barnes (1986). At high reaction temperature ($\leqslant$50 °C), deviation from linear dependence was observed and assumption of a first order rate is not valid. Changes in the contribution of different oxidizing species (e.g., HO$^\bullet$, Fe^{3+}, O_2) are inferred to control rates of pyrite dissolution at different temperatures.

The effect of temperature on the reaction rate is expressed by an Arrhenius relationship:

$$Ea = R * \partial(\log_e r)/\partial(1/T) \qquad (10)$$

where Ea is apparent Arrhenius activation energy (or critical increment of energy for a heterogeneous reaction), R is the universal gas constant, and T is temperature in Kelvin. Fig. 12 shows an Arrhenius plot of lnrate *vs.* 1/T for the reaction between H_2O_2 and pyrite in the temperature range of 4–150 °C. Within each Group of experiments, the rate of pyrite oxidation is strongly dependent on temperature, but it is difficult to cast the dependence into a simple Arrhenius equation because the value of the activation energy cannot be uniquely defined. The concave nature of the curves indicates that the activation energy decreases in high-tempera-
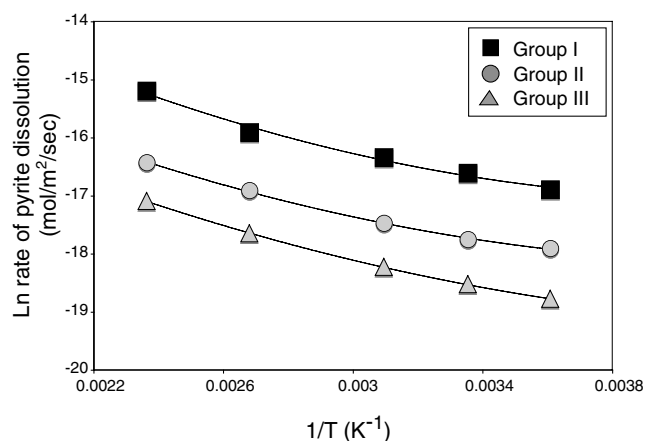
Fig. 12. Arrhenius plot of Ln (rate) as a function of inverse temperature for Group I, II, and III experiments run at temperature from 4 to 150 °C. The concave nature of the curves indicates that the activation energy decreases in high-temperature experiments, implying temperature-dependent mechanisms for pyrite oxidation.

ture experiments, implying temperature-dependent mechanisms for pyrite oxidation by H_2O_2.

Earlier studies recognized both O_2 and Fe^{3+} as effective oxidants for pyrite. Our data suggest that $HO^{\bullet}$ and O_2 are the most important oxidizing species resulting from H_2O_2 dissociation. Key controls for mechanisms and, therefore, rates of the oxidation of pyrite by $HO^{\bullet}$ are not known and cannot be determined by this study. Lowson (1982); Rosso et al. (1999a); Kamei and Ohmoto (1999); Rimstidt and Vaughan (2003); Borda et al. (2004) provide details on mechanisms of pyrite oxidation by molecular oxygen. Iron speciation in solution is also likely to play an important role in pyrite oxidation processes. At low pH (<3.5), Fe^{3+} is a more efficient oxidant than O_2, with rates of pyrite oxidation one order of magnitude higher for Fe^{3+} compared to O_2 (McKibben and Barnes, 1986; Bonnissel-Gissinger et al., 1998). Rates of reaction for a mixture of Fe^{3+} and O_2 are not a linear combination of rates law for Fe^{3+} and O_2 (Williamson and Rimstidt, 1994). In the case of pyrite oxidation by H_2O_2, the combination of H_2O_2-produced radicals, O_2, and Fe^{+3} aggressively oxidized pyrite surfaces. At high temperature, diffusion rates of oxidizing species to pyrite surfaces are high, as are rates of sulfate desorption and sulfate diffusion in solution. All of these factors contribute to the relatively fast rate of pyrite oxidation in high-temperature, sealed-tube experiments.

5.4. Interpretation of sulfur isotope values

A general reaction that summarizes the distribution of sulfur species during experimental pyrite oxidation is:

$$FeS_2 + H_2O_2 \rightarrow SO_4^{2-} + FeSO_4 + \{S^0 + S^n\} \qquad (11)$$

To calculate a sulfur isotope mass balance we considered initial pyrite (ip) as the sole sulfur reactant component. Sulfur product components were aqueous sulfate (aq), sulfate minerals (mm), elemental sulfur/polysulfide fraction (el)

and residual pyrite (rp). An isotopic mass balance may be expressed in terms of the mole fraction of sulfur contributed by each species as follow:

$$\delta^{34}S_{ip} = f_{aq} * \delta^{34}S_{aq} + f_{mn} * \delta^{34}S_{mn} + f_{el} * \delta^{34}S_{el}$$
$$+ f_{rp} * \delta^{34}S_{rp} \qquad (12)$$

Since $\delta^{34}S_{ip}$ is identical to $\delta^{34}S_{rp}$, the following equivalent equation may be written:

$$f_{aq}\varDelta^{34}S_{aq} + f_{mn}\varDelta^{34}S_{mn} + f_{el}\varDelta^{34}S_{el} = 0 \qquad (13)$$

Where $\varDelta$ is the difference between the initial isotopic value of pyrite and the final isotopic value of the sulfur products ($\varDelta^{34}S_{aq}$, $\varDelta^{34}S_{mn}$, and $\varDelta^{34}S_{el}$). Values measured were $\varDelta^{34}S_{aq} = +0.5$ to $+1‰$, $\varDelta^{34}S_{mn} = +0.8$ to $+1.5‰$ and $\varDelta^{34}S_{el}$ up to $-1.5‰$. Results from all experiments using average $\delta^{34}S$ values are given in Table 4.

In low-temperature experiments, mass balance calculations indicate that ^{34}S-enriched sulfates are balanced by ^{34}S-depleted elemental sulfur. Isotope mass balance calculations did not close for high-temperature experiments, with 4–11% of the ^{32}S-enrichment fraction not accounted. The experiments that did not isotopically balance were those in which significant amounts of hematite were produced. As mentioned above, electron microprobe analyses identified 7–12 wt% sulfur in hematite crystals. Repeated stable isotope analyses of hematite flakes showed consistently low $\delta^{34}S$ values of -1.6 to $+1.4‰$. Consequently, we hypothesize that a fraction of the ^{32}S-enriched fraction was disseminated within hematite crystals.

Stable isotope results of this study indicate that pyrite oxidation by H_2O_2 induces similar isotopic fractionation to that recognized in previous studies (e.g., Taylor et al., 1984; Toran and Harris, 1989). $\delta^{34}S$ of pyrite remains unchanged during the oxidation process, but enrichments in produced sulfate and depletions in elemental sulfur are observed. Experimental abiotic fractionations of sulfur isotope between reactant pyrite and oxidation products are not large, but indicate that an isotopically distinct sulfate is produced during oxidation. Fractionation is inferred to result from formation of intermediate complexes involving numerous side reactions and disproportionation reactions (Rimstidt and Vaughan, 2003). It is notable, however, in our experiments that intermediate sulfoxyanions were not recovered.

This experimental study shows that reactions associated with radiolysis are unlikely to change $\delta^{34}S$ of source pyrite, but can produce ^{34}S-enriched sulfates. In natural environments, additional processes might occur and further alter sulfur isotope values. Microbial reduction and disproportionation of radiolytically produced sulfur species could create secondary pyrite with sulfur isotope signatures distinct from that of a uniform sulfur reservoir such as the mantle. Rapid, but abiotic, disproportionation to sulfate and sulfide has been proposed by Warren (1972) to explain ^{34}S-depleted pyrite in the ore-zone of roll-front-type sandstone-hosted uranium deposits. In light of our current

results, microbial metabolisms should be investigated for producing ^{34}S-depleted pyrite during reduction and disproportionation reactions. Consequently, study of sulfur isotope signatures may be crucial for distinguishing between chemical gradients that sustain microbial life and chemical gradients that sustain abiotic reactions.

6. Implications of pyrite oxidation by H_2O_2

Gaseous, aqueous, and solid products from experimental reactions between H_2O_2 and pyrite provide insightful analogues for water–rock reactions in natural environments where radiolysis occurs as a result of the decay of radionuclides (e.g. uranium deposits) or ionizing irradiation (e.g. Europa ice surface). These experiments reveal a surprising array of dissolution features as well as aqueous and solid products from decomposition of pyrite at a specific concentration of oxidant. Ferrous ions, sulfide species, elemental sulfur, and sulfoxyanions appear to be active sources of transferable electrons in sealed-tube H_2O_2 experiments. If the oxidizing potential is sufficient for pyrite decomposition then accessibility of pyrite surface, pH, and competition among thermodynamically favorable reactions are inferred to be dominant factors influencing observed experimental products. In natural settings on Earth, additional important influences on supply and fate of radiolytic oxidants are mineral composition, mineral concentration, composition of dissolved species, mass transport parameters, and microbiology.

Molecular oxidants such as H_2O_2 and O_2 are generally reported at μg/L levels or below detection levels in groundwaters associated with uranium-bearing gold ores or high-grade uranium deposits even when dissolved hydrogen is reported at levels of mg/L (Liu et al., 1996; Lin et al., 2005). Our experimental findings are consistent with dissolved hydrogen being more mobile and less reactive than H_2O_2 or O_2 (Lin et al., 2005). Assuming mass conservation, hydrogen release can be used to estimate production of oxidants during radiolysis in the subsurface. It remains to be determined, however, if abiotic or biotic reactions are the dominant sink for radiolytic oxidants in the subsurface of Earth. At temperatures near freezing, biotic reactions are kinetically more favorable than abiotic reactions and cycling mechanisms involving multiple reactive species of iron and sulfur can be viewed as potential energy sources for sustained microbiological activity.

Rapid recombination rates for photolysis products in the Mars atmosphere are inferred widely as the explanation for CO_2 being the primary atmospheric constituent and for relatively low concentrations of CO, O_2, and O_3 (e.g. Krasnopolsky, 2003). Roles of specific catalytic components, such as metals or HOx, within the lower Martian atmosphere are difficult to evaluate due to low concentrations of reactants and widely variable abundance of water vapor. Trace-level concentrations of H_2O_2 in the Mars atmosphere have been measured recently using mid-infrared (Encrenaz et al., 2004) and sub-millimeter spectroscopy (Clancy et al., 2004) employing ground-based telescopes. Global atmospheric temperature variations are large on Mars due to orbital eccentricity and associated large variations in latitudinal and vertical gradients of H_2O (Jakosky and Farmer, 1982; Smith, 2002) and H_2O_2 (Clancy et al., 2004). Although H_2O_2 is generally regarded as of little or no geochemical significance on Earth, it is increasingly clear that the H_2O_2 molecule plays a pivotal role in Martian atmospheric and soil chemistry. In anticipation of Mars sample return and human exploration of Mars, experimental and field studies are needed to assess hydrogeochemical, lithogeochemical, and biogeochemical cycling of H_2O_2 on Earth.

Acknowledgments

Associate editor: Martin B. Goldhaber

References

Allen, A.O., 1961. *The Radiation Chemistry of Water and Aqueous Solutions*. Van Nostrand, New York.

Alpers, C.N., Blowes, D.W. 1994, Environmental Geochemistry of Sulfide Oxidation. ACS Symp. Ser. 550. American Chemical Society, Washington DC.

Amme, M., 2002. Contrary effects of the water radiolysis product H_2O_2 upon the dissolution of nuclear fuel in natural ground water and deionized water. *Radiochimica Acta* **90**, 399–406.

Becker, U., Rosso, K.M., Hochella, M.F., 2001. The proximity effect on semiconducting mineral surfaces: a new aspect of mineral surface reactivity and surface complexation theory?. *Geochim. Cosmochim. Acta* **65** 2641–2649.

Billault, V., Beaufort, D., Patrier, P., Petit, S., 2002. Crystal chemistry of Fe-sudoites from uranium deposits in the Athabasca basin (Saskatchewan, Canada). *Clay. Clays Miner.* **50**, 70–81.

Bonnissel-Gissinger, P., Alnot, M., Ehrhardt, J.J., Behra, P., 1998. Surface oxidation of pyrite as a function of pH. *Environ. Sci. Technol.* **32**, 2839–2845.

Borda, M.J., Strongin, D.R., Schoonen, M.A., 2004. A vibrational spectroscopic study of the oxidation of pyrite by molecular oxygen. *Geochim. Cosmochim. Acta* **68**, 1807–1813.

Bottcher, M., Thamdrup, B., Vennemann, T., 2001. Oxygen and sulfur isotope fractionation during anaerobic bacterial disproportionation of elemental sulfur. *Geochim. Cosmochim. Acta* **65**, 1601–1609.

Brüchert, V., Pratt, L.M., 1996. Contemporaneous early diagenetic formation of organic and nonorganic sulfur in estuarine sediments from St. Andrew Bay, Florida, USA. *Geochim. Cosmochim. Acta* **60**, 2325–2332.

Bruneton, P., 1994. Geology of the Cigar Lake uranium deposit (Saskatchewan, Canada). In: Gilboy, C.F., Vigrass, L.W. (Eds.), Economic Minerals of Saskatchewan. *Sask. Geol. Soc. Spec. Publ.* **8**, pp. 99–199.

Buckley, A.N., Riley, K.W., 1991. Self-induced floatability of sulphide minerals: examination of recent evidence for elemental sulphur as the hydrophobic entity. *Surf. Interf. Anal.* **17**, 655–659.

Budakoglu, M., Pratt, L.M., 2005. Sulfur-isotope distribution and contamination related to the Balya Pb–Zn in Turkey. *Environ. Geol.* **47**, 773–781.

Burns, P.C., Hughes, K.A., 2003. Studtite, $[(UO_2)(O_2)(H_2O)_2](H_2O)_2$: the first structure of a peroxide mineral. *Am. Mineral.* **88**, 1165–1168.

Buxton, G.V. 1987. In: Radiation Chemistry: Principles and Applications; Farhataziz, Rodgers, M.A.J., Eds. VCH Publishers: New York, p 321.

Canfield, D.E., Thamdrup, B., Fleischer, S., 1998. Isotope fractionation and sulfur metabolism by pure and enrichment cultures of elemental sulfur-disproportionating bacteria. *Limnol. Oceanogr.* **43**, 253–264.

Canfield, D.E., Habicht, K.S., Thamdrup, B., 2000. The archean sulfur cycle and the early history of atmospheric oxygen. *Science* **288**, 658–661.

Canfield, D.E., 2001. Biochemistry of sulfur isotopes. In: Valley, J.V., Cole, D.R. (Eds.), Stable Isotope Geochemistry; *Rev. Miner. Geochem.*, **43**, pp. 607–636.

Carlson, R.W., Anderson, M.S., Johnson, R.E., Schulman, M.B., Yavrouian, A.H., 2002. Sulfuric acid production on Europa: the radiolysis of sulfur in water ice. *Icarus* **157**, 456–463.

Chen, G., Zen, F., Fan, F., Bard, A.J., 1991. Electrochemical investigation of the energetic of irradiated FeS_2 (pyrite) particles. *J. Phys. Chem.* **95**, 3682–3687.

Chyba, C.F., 2000. Energy for microbial life on Europa. *Nature* **406**, 368.

Clarke, P.J., Fogwill, W.D., 1985. Geology of the Dawn Lake uranium deposits, northern Saskatchewan. In: Sibbald, T.I.I., Petruk, W. (Eds.), Geology of Uranium Deposits. *Can. Inst. Min. Metall. Spec.*, **32**, pp. 132–139.

Clancy, R.T., Sandor, B.J., Moriarty-Schieven, G.H., 2004. A measurement of the 362 GHz absorption line of Mars atmospheric H_2O_2. *Icarus* **168**, 116–121.

Druschel, G.K., Hamers, R.J., Luther, G.W., Banfield, J.F., 2004. Kinetics and mechanism of trithionate and tetrathionate oxidation at low pH by hydroxyl radicals. *Aqueous Geochem.* **9**, 145–164.

Dubessy, J., Pagel, M., Beny, J.M., Christensen, H., Hickel, B., Kosztolanvi, C., Poty, B., 1988. Radiolysis evidenced by H_2O_2 and H_2-bearing fluid inclusions in three uranium deposits. *Geochim. Cosmochim. Acta* **52**, 1155–1167.

Encrenaz, T., Bézard, B., Greathouse, T.K., Richter, M.J., Lacy, J.H., Atreya, S.K., Wong, A.S., Lebonnois, S., Lefèvre, F., Forget, F., 2004. Hydrogen peroxide on Mars: evidence for spatial and seasonal variations. *Icarus* **170**, 424–429.

Ermakov, A.N., Poskrebyshev, G.A., Purmal, A.P., 1997. Sulfite oxidation: the state-of- the-art of the problem. *Kinet. Catal.* **38**, 295–308.

Evangelou, V.P., 1995. *Pyrite Oxidation and its Control*. CRC Press, Boca Raton, FL.

Fayek, M., Janeczek, J., Ewing, P.C., 1997. Mineral chemistry and oxygen isotopic analyses of uraninite, pitchblende and uranium alteration minerals from the Cigar Lake deposit, Saskatchewan, Canada. *Appl. Geochem.* **12**, 549–565.

Garrett, B.C., 45 others, 2004. Role of Water in Electron-Initiated Processes and Radical Chemistry: Issues and Scientific Advances. *Chem. Rev.* **105**, pp. 355–390.

Goldhaber, M.B., 1983. Experimental study of metastable sulfur oxyanion formation during pyrite oxidation at pH 6–9 and 30 °C. *Am. J. Sci.* **238**, 193–217.

Gomis, O., Satorre, M.A., Strazzulla, G., Leto, G., 2004. Hydrogen peroxide formation by ion implantation in water ice and its relevance to the Galilean satellites. *Planet. Space Sci.* **52**, 371–378.

Grotzinger, J.P., Knoll, A.H., 1999. Stromatolites in Precambrian carbonates: evolutionary mileposts or environmental dipsticks? *Ann. Rev. Earth Planet. Sci.* **27**, 313–358.

Guevremont, J.M., Bebie, J., Elsetinow, A.R., Strongin, D.R., Schoonen, M.A.A., 1998. Reactivity of the (100) plane of pyrite in oxidizing gaseous and aqueous environments: effects of surface imperfections. *Environ. Sci. Technol.* **32**, 3743–3748.

Habicht, K., Canfield, D.E., Rethmeier, J., 1998. Sulfur isotope fractionation during bacterial reduction and disproportionation of thiosulfate and sulfite. *Geochim. Cosmochim. Acta* **62**, 2585–2595.

Hiroki, A., LaVerne, J.A., 2005. Decomposition of hydrogen peroxide at water–ceramic oxide interfaces. *J. Phys. Chem. B* **109**, 3364–3370.

Holland, H.D., 1994. Early Proterozoic atmospheric change. In: Bengston, S. (Ed.), *Early Life on Earth*. Columbia University Press, New York, pp. 237–244.

Jakosky, B.J., Farmer, C.B., 1982. The seasonal and global behavior of water vapor in the Mars atmosphere: complete global results of the Viking atmospheric water detector experiment. *J. Geophys. Res.* **87**, 2999–3019.

Jerz, J., Rimstidt, J.D., 2004. Pyrite oxidation in moist air. *Geochim. Cosmochim. Acta* **68**, 701–714.

Kamei, G., Ohmoto, H., 1999. The kinetics of reactions between pyrite and O_2-bearing water revealed from in situ monitoring of DO, Eh and pH in a closed system. *Geochim. Cosmochim. Acta* **64**, 2585–2601.

Kendelewicz, T., Doyle, C.S., Bostick, B.C., Brown, G.E., 2004. Initial oxidation of fractured surfaces of FeS_2 (1 0 0) by molecular oxygen, water vapor, and air. *Surf. Sci.* **558**, 80–88.

Krasnopolsky, V.A., 2003. Spectroscopic mapping of the CO mixing ratio: detection of seasonal asymmetry. *J. Geophys. Res.* **108**, 1–13.

Krouse, H.R., Gould, W.D., McCready, R.G.L., Rajan, S., 1991. [18]O incorporation into sulphate during bacterial oxidation of sulphide minerals and the potential for oxygen isotope exchange between O_2, H_2O and oxidized sulphur intermediates. *Earth Planet. Sci. Lett.* **107**, 90–94.

Lin, L.H., Slater, G.F., Sherwood Lollar, B., Lacrampe-Couloume, G., Onstott, T.C., 2005. The yield and isotopic composition of radiolytic H_2, a potential energy for the deep subsurface biosphere. *Geochim. Cosmochim. Acta* **69**, 893–903.

Lowson, R.T., 1982. Aqueous pyrite oxidation by molecular oxygen. *Chem. Rev.* **82**, 461–497.

Liu, J., Yu, J.W., Neretnieks, I., 1996. Transport modeling in the natural analogue study of the Cigar Lake uranium deposit (Saskatchewan, Canada). *J. Contam. Hydro.* **21**, 19–34.

Luther III, G.W., 1987. Pyrite oxidation and reduction: molecular orbital theory considerations. *Geochim. Cosmochim. Acta* **51**, 3193–3199.

McKibben, M.A., Barnes, H.L., 1986. Oxidation of pyrite in low temperature acidic solutions: rate laws and surface textures. *Geochim. Cosmochim. Acta* **50**, 1509–1520.

Moses, C.O., Nordstrom, D.K., Herman, J.S., Mills, A.L., 1987. Aqueous pyrite oxidation by dissolved oxygen and ferric iron. *Geochim. Cosmochim. Acta* **51**, 1561–1571.

Mycroft, J.R., Bancroft, G.M., Mcintyre, N.S., Lorimer, J.W., Hill, I.R., 1990. Detection of sulfur and polysulfides on electrochemically oxidized pyrite surfaces by X-ray photoelectron spectroscopy and Raman spectroscopy. *J. Electroanal. Chem.* **292**, 139–152.

Nesbitt, H.W., Bancroft, G.M., Pratt, A.R., Scaini, M.J., 1998. Sulfur and iron surface states on fractured pyrite surfaces. *Am. Mineral.* **83**, 1067–1076.

Nesbitt, H.W., Scaini, M., Hochst, H., Bancroft, G.M., Schaufuss, A.G., Szargan, R., 2000. Synchrotron XPS evidence for Fe^{2+}–S and Fe^{3+}–S surface species on pyrite fracture surfaces, and their 3d electronic states. *Am. Mineral.* **85**, 850–857.

Nordstrom, D.K., Alpers, C.N., 1999. Geochemistry of acid mine waters. In: Plumlee, G.S., Logsdon, M.J. (Eds.), *The Environmental Geochemistry of Mineral Deposits*. Society of Economic Geologists, Littleton, CO, pp. 133–160.

Ohmoto, H., 2004. Archean atmosphere, hydrosphere, and biosphere. In: Erickson P. (Ed.), The Precambrian Earth: Tempos in Precambrian. *Dev. Precambrian Geol.*, **12**, pp. 361–368, Elsevier.

Pastina, B., LaVerne, J.A., 2001. Effect of molecular hydrogen on hydrogen peroxide in water radiolysis. *J. Phys. Chem. A* **105**, 9316–9322.

Petrik, N.G., Alexandrov, A.B., Vall, A.I., 2001. Interfacial energy transfer during gamma radiolysis of water on the surface of ZrO_2 and some other oxides. *J. Phys. Chem. B* **105**, 5935–5944.

Reedy, B.J., Beattie, J.K., Lowson, R.T., 1991. A vibrational spectroscopic ^{18}O tracer study of pyrite oxidation. *Geochim. Cosmochim. Acta* **55**, 1609–1614.

Rimstidt, J.D., Vaughan, D.J., 2003. Pyrite oxidation: a state-of the-art assessment of the reaction mechanism. *Geochim. Cosmochim. Acta* **67**, 873–880.

Rosso, K.M., Becker, U., Hochella Jr., M.F., 1999a. Atomically resolved electronic structure of pyrite {100} surfaces: an experimental and theoretical investigation with implications for reactivity. *Am. Mineral.* **84**, 1535–1548.

Rosso, K.M., Becker, U., Hochella Jr., M.F., 1999b. The interaction of pyrite {100} surfaces with O2 and H$_2$O: fundamental oxidation mechanisms. *Am. Mineral.* **84**, 1549–1561.

Rye, R.O., Bethke, P.M., Wasserman, M.D., 1992. The stable isotope geochemistry of acid sulfate alteration. *Econ. Geol.* **87**, 225–262.

Sasaki, K., 1994. Effect of grinding on the rate of pyrite oxidation by oxygen in acid solution. *Geochim. Cosmochim. Acta* **58**, 4649–4655.

Sasaki, K., Tsunekawa, M., Tanaka, S., Konno, H., 1995. Confirmation of a sulfur-rich layer on pyrite after oxidative dissolution by Fe(III) ions around pH 2. *Geochim. Cosmochim. Acta* **59**, 3155–3158.

Savary, V., Pagel, M., 1997. The effects of water radiolysis on local redox conditions in the Oklo, Gabon, natural fission reactors 10 and 16. *Geochim. Cosmochim. Acta* **61**, 4479–4494.

Schippers, A., Jørgensen, B.B., 2001. Oxidation of pyrite and iron sulfide by manganese dioxide in marine sediments. *Geochim. Cosmochim. Acta* **65**, 915–922.

Schaufuss, A.G., Nesbitt, H.W., Kartio, I., Laajalehto, K., Bancroft, G.M., Szargan, R., 1998. Reactivity of surface chemical states on fractured pyrite. *Surf. Sci.* **411**, 321–328.

Schöneshöfer, M., 1973. Pulsradiolytische untersuchung über das S$_4$O$_3^-$ radikal als wischenprodukt der thiosulfatoxidation und tetrathionatreduktion. *Int. J. Radiat. Phys. Chem.* **5**, 375–386.

Seal, R.R. II, 2003. Stable-isotope geochemistry of mine waters and related solids. In: Jambor J.L., Blowes D.W., Ritchie A.I.M. (Eds.), Environmental Aspects of Mine Wastes. *Mineral. Assoc.* Short Course **31**, pp. 303–334.

Seal, R.R. II, Wandless, G.A., 1997. Stable isotope characteristics of waters draining massive sulfide deposits in the eastern United States. In: Wanty, R.B., Marsh, S.P., Gough, L.P., (Eds.), Fourth International Symposium on Environmental Geochemistry, *Proceedings U.S. Geol. Surv.* Open-File Report **97**, p. 496.

Smith, M.D., 2002. The annual cycle of water vapor on Mars as observed by the thermal emission spectrometer. *J. Geophys. Res.* **107**, 25.1–25.19.

Spinks, J.W.T., Woods, R.J., 1990. *An Introduction to Radiation Chemistry*, third ed. Wiley, New York.

Stefanic, I., LaVerne, J.A., 2002. Temperature dependence of the hydrogen peroxide production in the radiolysis of water. *J. Phys. Chem. A.* **106**, 447–452.

Sweeney, R.E., Kaplan, I.R., 1973. Pyrite framboid formation; laboratory synthesis and marine sediments. *Econom. Geol.* **68**, 618–634.

Taylor, B.E., Wheeler, M.C., 1994. Sulfur and oxygen-isotope geochemistry of acid mine drainage in the western United States. In: (Alpers, C.N., Blowes, D.W., (Eds.), Environmental Geochemistry of Sulfide Oxidation. *Am. Chem. Soc. Symp. Ser.* **550**, pp. 481–514.

Taylor, B.E., Wheeler, M.C., Nordstrom, D.K., 1984. Isotope composition of sulfate in acid mine drainage as measure of bacterial oxidation. *Nature* **308**, 538–541.

Todd, E.C., Sherman, D.M., Purton, J.A., 2003. Surface oxidation of pyrite under ambient atmospheric and aqueous (pH 2 to 10) conditions: electronic structure and mineralogy from X-ray absorption spectroscopy. *Geochim. Cosmochim. Acta* **67**, 881–893.

Toran, L., Harris, R., 1989. Interpretation of sulfur and oxygen isotopes in biological and abiological sulfide oxidation. *Geochim. Cosmochim. Acta* **53**, 2341–2348.

Usher, C.R., Paul, K.W., Narayansamy, J., Strongin, D., 2005. Mechanistic aspects of pyrite oxidation in an oxidizing gaseous environment: an in situ HATR-IR isotope study". *Environ. Sci. Technol.* **39** (19), 7576–7584.

Vovk, I.F., 1982. Radiolysis of underground waters as the mechanism of geochemical transformation of the energy of radioactive decay in sedimentary rocks. *Litho. Mineral. Res.* **16**, 328–334.

Vovk, I.F., 1987. Radiolytic oxidation of sulphides and geochemical behavior of sulfur isotopes in uranium deposits. In: Studies on sulphur isotope variations in nature. International Atomic Energy Agency, Vienna, Austria, pp. 85–103.

Warren, C.G., 1972. Sulfur isotopes as a clue to the genetic geochemistry of roll-type uranium deposit. *Econ. Geol.* **67**, 759–767.

Williamson, M.A., Rimstidt, J.D., 1994. The kinetics and electrochemical rate determining step of aqueous pyrite oxidation. *Geochim. Cosmochim. Acta* **58**, 5443–5454.

Wächtershäuser, G., 2000. Life as we don't know it. *Science* **289**, 1307–1308.

Weiss, B., Yung, Y.L., Nealson, K.H., 2000. Atmospheric energy for subsurface life on Mars? *Proc. Natl. Acad. Sci. USA* **97**, 1395–1399.